COMPARISON OF DYNAMIC WAKE MODELS WITH CLOSED-FORM OPTIMUM PROPELLER SOLUTIONS

Stephen M. Makinen and David A. Peters
Department of Mechanical and Aerospace Engineering
Washington University
Saint Louis, U.S.A.

Abstract

The following article explains how to extend the He-Peters dynamic wake model to be applicable to propellers with a large swirl velocity component. Dynamic wake model calculations accurately predict the inflow behavior for helicopter rotors, including axial flow for large tip-speed ratios ($(\Omega R/V_\infty) \geq 20$). The swirl velocity is a prominent component for small tip-speed ratios (≤ 5), typical of forward flight for tiltrotor craft such as the V-22 Osprey and the BA609. Results for dynamic wake calculations are compared to the classic analytic solutions for optimally efficient propellers by Prandtl and Goldstein. The exact and approximate solutions correlate strongly for infinite-blade cases, and finite blade cases with a large tip-speed ratio. The He-Peters dynamic wake model converges poorly, for small tip-speed ratios, due to neglect of the swirl velocity at the inboard blade region. A derivation is presented for adapting the mass matrix, with an empirical factor, to account for the nonzero mass at the blade root. Results from the modified dynamic wake model correlate well with the two-dimensional exact solution, based on a chosen optimal value for the empirical factor. The error norm for the modified He-Peters model, versus Prandtl's solution, remains constant at approximately 3% for tip-speed ratio range, $5 \leq \mu_0 \leq 20$. The error norm diverges to large values in a concerted manner for $\mu_0 < 5$. The applicable range of the He-Peters dynamic wake model for axial flow is greatly expanded by substituting the modified mass matrix into the calculation equations. An optimal empirical value can also be chosen for convergence with Goldstein's solution at the medial and outboard blade regions, but further research is required to include the far inboard vortex effects present in the three-dimensional exact solution.

Nomenclature

a_m	Goldstein solution coefficient
$[A^m_{jn}]$	Area Matrix, He-Peters Model
$[B^m_{jn}]$	B-Matrix, He-Peters Model
e_ν	Error Norm in the domain $\nu \in [0,1]$
$[E^{m0}_{nj}]$	expansion transformation matrix
$\mathcal{E}$	set of all even integers, $\{0,2,4,\ldots\}$
$[I]$	identity matrix
I_ζ	modified Bessel function of the first kind
j,n	Legendre function Degree indices
k	empirical factor for modified mass matrix, $[M^{mr}_{nj}]$
K_ζ	modified Bessel function of the second kind
$[K^m_n]$	original axial flow He-Peters model mass matrix
L	non-dimensional lift per unit length on an individual propeller blade, function of radius
m,r	Legendre function order indices
m_{max}	maximum Legendre function order index for a truncated series
$[M^{mr}_{nj}]$	modified mass matrix
N	number of terms for Goldstein solution
N_m	number of terms for the mth order Legendre function expansion
$\mathcal{N}_m$	maximum degree index for Legendre expansion of the mth order
O	set of all odd integers, $\{1,3,5,\ldots\}$
p	non-dimensional pressure field, $p = P/(\rho\Omega^2 R)$
P	dimensional pressure field
$\bar{P}^m_n$	normalized associated Legendre function of the first kind
q	index specifying the qth blade, $q \in \{1,2,\ldots\}$
Q	number of propeller blades
$\bar{Q}^m_n$	normalized associated Legendre function of the second kind
$\bar{r}$	non-dimensional radial coordinate
R	propeller radius (dimensional)
$S_{\kappa,\zeta}$	Lommel function
$T_{\kappa,\zeta}$	finite real-valued portion of Lommel function
$\vec{v}$	non-dimensional velocity vector (dimensionless on ΩR)
v_∞	non-dimensional free-stream velocity, $v_\infty = V_\infty/(\Omega R)$
V_∞	free-stream velocity (dimensional)
w_0	induced vertical velocity component on propeller disk (dimensionless on ΩR)
w_B	Betz induced velocity distribution in far wake (dimensionless on ΩR)
α^m_n, β^m_n	velocity field expansion coefficients, non-rotating coordinate system
$\hat{\alpha}^m_n, \hat{\beta}^m_n$	velocity field expansion coefficients, rotating coordinate system
$\delta()$	Dirac's delta function
δ_{jn}	Kronecker delta matrix
$\bar{\Gamma}$	non-dimensional normalized circulation

$\bar{\Gamma}_p$	Prandtl's circulation solution
$\bar{\Gamma}_g$	Goldstein's circulation solution
$\bar{\Gamma}_{gm}$	modified Goldstein circulation solution
$\eta, \nu, \hat{\psi}$	ellipsoidal coordinates in the rotating system
λ	inflow ratio $\lambda = V_\infty/\Omega R$ (dimensionless)
μ	blade-speed ratio, change of variable for radial coordinate, $\mu = \mu_0 \bar{r}$ on the propeller blade
μ_0	tip-speed ratio $\mu_0 = \Omega R/V_\infty$ (dimensionless)
ξ	free-stream coordinate (dimensionless on R)
ρ	density (dimensional)
τ	non-dimensional time, $\tau = t\Omega$
τ_n^{mc}, τ_n^{ms}	pressure field expansion coefficients, non-rotating system
$\hat{\tau}_n^{mc}, \hat{\tau}_n^{ms}$	pressure field expansion coefficients, rotating system
ϕ	thrust vector tilt-angle off vertical axis
$\bar{\psi}$	ellipsoidal azimuthal coordinate in the non-rotating coordinate system
$\hat{\psi}$	ellipsoidal azimuthal coordinate in the rotating system
ψ_q	azimuthal angle for the qth blade in the rotating coordinate system
Ω	propeller rotational rate
ΩR	propeller tip-speed
$\frac{\partial}{\partial \bar{\xi}}$	partial derivative along free-stream coordinate
$(\hat{\ })$	rotating coordinate system
$(\bar{\ })$	normalized parameter, except for $\bar{\psi}$
$[\ ]^T$	matrix transpose
$[\ ]^{-1}$	matrix inverse
$\{\ \}$	vertical vector quantity

Introduction

Aerodynamic characteristics for axial flow of helicopter rotors and airplane propellers for axial flow must be taken into account in applied aerodynamic models. The modelling techniques must reflect the appropriate dominant characteristics for the given flight conditions. Axial flow for helicopter rotors and airplane propellers typically has an advance ratio (tip-speed ratio) of $\lambda = 0.033$ ($\mu_0 = 30$) to $\lambda = 1.0$ ($\mu_0 = 1.0$). The maximum vertical ascent rate for a helicopter has an approximate inflow ratio $\lambda = 0.15$ ($\mu_0 = 6.6$), while propellers can operate with an inflow ratio $\lambda = 1.0$ ($\mu_0 = 1.0$). For example, the BA609 tiltrotor craft cruises in airplane mode in a range from approximately 77kts ($\mu_0 = 5$) to a maximum speed of 275kts ($\mu_0 = 1.4$).

Dynamic wake models were originally developed for helicopter rotors in axial and skewed flow (Ref 9, 14, 15, 18, 19). Correlation with other data has not been done for large inflow ratios in axial flow. The swirl velocity component becomes more prominent in this flight regime as does the slope of the trailing vortex as it sheds off the propeller blades. Research into developing the dynamic wake models has so far neglected the effects of a prominent swirl velocity component. A major goal of this project is to include the swirl component in an effort to extend the range of application for the dynamic wake models.

Previous Work Albert Betz developed an extended form of momentum theory in 1919 to describe the most efficient inflow for a lightly loaded propeller (Ref 4). Betz showed that the most efficient induced velocity inflow creates trailing vortices that form a regular helical sheet from each blade. The helix geometry remains constant along it's axis and does not exhibit characteristics of slipstream contraction. No concentrated vortices exist at the root or tip of the blade, either. A lightly loaded propeller is defined as one with *many* blades and *small* thrust vectors (Ref 5, page 255). The optimal vortex geometry is shown in figure 1 for a two-bladed propeller. Betz showed that the vorticity, for the optimum propeller, will trail the propeller like a rigid screw surface moving in translation downstream of the propeller.

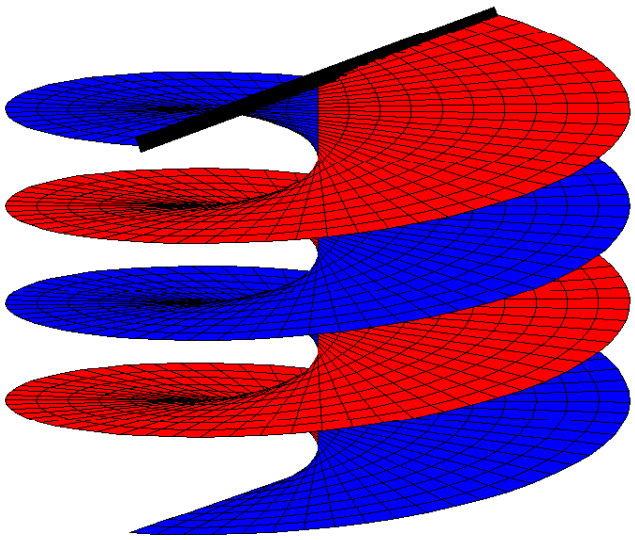

Figure 1: Optimal Trailing Vortex Geometry determined by A. Betz (Ref 4)

The sheet of vorticity from the blade is composed of little vortices shed off the blade azimuthally as the thrust varies in the radial direction. The air flows into the propeller with a free-stream velocity V_∞. The tangential velocity component of the airflow is Ωr. The slope of the helix at a given radial distance, r, is $V_\infty/\Omega r$. The inflow ratio at the blade-tip becomes $v = V_\infty/\Omega R$. The tip-speed ratio is defined as the reciprocal of the inflow ratio, or $\mu_0 = \Omega R/V_\infty$ and is useful for a change of variable that scales the radial coordinate, $\bar{r}$. The wake spacing is classically defined as the dimensionless distance scale between two successive vortex sheets and is calculated as, $s = 2\pi/Q\mu_0$.

The optimal induced velocity on the blade is found by

determining the profile that would create the helix geometry that Betz described. The radial distribution along the length of the blade is the same as the radial distribution for an infinite-blade propeller (Fig 2).

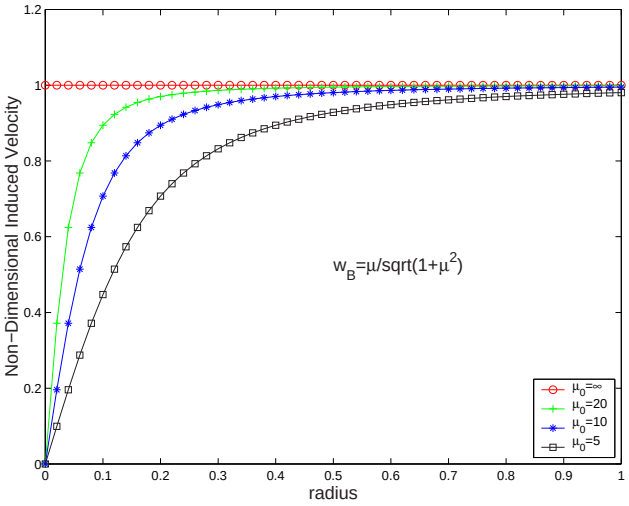

Figure 2: Optimal Radial Velocity Distribution Along Blade, determined by A. Betz

The appendix to Betz's paper includes a two-dimensional exact solution, determined by Prandtl, to the circulation around an ideal propeller blade. Circulation at the blades was determined by analyzing the vortex sheets in the far wake (Ref 11) of the optimal trailing vortex geometry. The number of physical dimensions was reduced by neglecting the finite radius of the actuator disk. The solution was formulated from a model of semi-infinite parallel vortex sheets in the far wake, which also inherently neglects the tilt angle of the thrust vector at the inboard region of the blade. The vertical separation between sheets in Prandtl's model corresponds to the wake spacing distance for a three-dimensional helix. Prandtl's circulation solution consists of the infinite blade solution with a decay multiplier. The resulting solution shows characteristics of an infinite-blade propeller inboard and of a finite blade propeller outboard.

Goldstein studied the reverse problem of optimal wake geometry by solving Laplace's equation for the velocity potential for the fluid motion between the vortex sheets. The Betz velocity distribution at the sheets was used as the boundary condition. The radial circulation profile was then determined from the velocity potential solution. The circulation solution to maintain optimal vortex geometry can be applied to an optimal propeller since the circulation does not change along the axis of the trailing vortex helix.

The solutions by Prandtl and Goldstein show excellent agreement for larger tip speed ratios (Ref 6). Prandtl's model agrees with that of Goldstein closer to the blade tip, which is due to the dependance of Prandtl's solution on the tip-loss factor. Prandtl's solution also overshoots Goldstein's solution at the medial blade region. Prandtl's clever dimensional reduction approach illustrates the significance of outboard vorticies over inboard vortices, although this dominant relationship is only true for large tip-speed ratios, μ_0. Wayne Johnson (Ref 11) describes that Prandtl's solution is generally found to be a good approximation to Goldstein's solution for wake spacing, $s \leq 0.63$, or in terms of the tip-speed ratio for two- and four-bladed propellers, $\mu_0 \geq 5$ and $\mu_0 \geq 2.5$ respectively. The classic aerodynamic solutions are also summarized by Glauert (Ref 5, p. 251-258). A large body of Russian research on airscrews is summarized in a NASA technical translation (Ref 3).

Hall and Yang developed a method to solve for minimum-induced loss by utilizing a generalized form of the Betz vortex geometry for forward flight. A lightly loaded propeller is described as one where the induced velocities are small compared to the propeller velocity (Ref 8, page 839). Describing the system in this manner implies that the trailing vortex sheet will be undistorted by the induced flow for a considerable distance behind the propeller, and the trailing vortex can be modelled as a rigid body translating downstream. The justifying descriptions of using a rigid wake model by Hall and Yang are useful for conceptualization and are equivalent to the original statements by Betz.

Recent Developments Ormiston and Peters derived unsteady induced flow perturbation equations for a helicopter rotor undergoing thrust, roll and pitch moments (Ref 16). The momentum-theory equations correlated well with rotor response data. Pitt and Peters (Ref 19) developed a low-order approximation to the induced velocity flow field, by extending Mangler's model (Ref 13) to create a dynamic inflow theory. The actuator disk model of Mangler was extended for unsteady aerodynamics of helicopter rotors in the time domain.

He and Peters further developed the Pitt-Peters model (Ref 17, 18) to create an unsteady, induced flow theory for helicopter rotors. The vertical component of the induced velocity and the pressure difference for the *on-disk* modes were expanded to create a dynamic wake model that could be coupled with blade dynamics and pilot control models.

Morillo expanded the dynamic wake model (Ref 15) to include three-dimensional velocity modes everywhere in the infinite hemisphere above the actuator disk by utilizing a more generalized expansion series for both the velocity and pressure fields.

Gomez attempted to reproduce the circulation results obtained by Prandtl and Goldstein for an optimally efficient propeller with the He-Peters model (Ref 7). The reverse problem of calculating the circulation from the ideal velocity inflow was attempted. Excellent agreement was obtained

for the infinite blade case, but no satisfactory results were obtained for finite blade cases of higher free-stream velocities ($\mu_0 < 20$). Good correlation between Gomez's results and that of Prandtl and Goldstein was obtained for lower free-stream velocities ($\mu_0 = 20$).

Present Approach The problem of determining the relationship between the velocity field and circulation around propeller blades has been solved previously by the aforementioned scientists. The current project aims to reproduce this relationship with the He-Peters model (Ref 17, 18). The classic aerodynamic solutions are based upon the trailing vortex system far downstream of the propeller. The current work with the dynamic wake models is based on an infinite hemisphere above the rotor and the actuator disk itself. Relating the phenomena at the propeller to the flow far downstream assists in expanding the dynamic wake models towards a more comprehensive tool set. An inflow model, without a coupled blade dynamics model, *should* reproduce the results of the optimally efficient solutions by Betz, Prandtl and Goldstein. Poor correlation between the exact solutions and dynamic wake model results could be traced to a fundamental problem with the assumptions in the derivation.

In previous studies, the He-Peters model was shown to give the correct swirl velocity for an infinite number of blades (Ref 2) even for large shedding angles of the vortex sheet ($\mu_0 \leq 5$). This correlation is obtained by the following application. The tilted blade lift on the propeller is placed normal to the actuator disk of the inflow model. The resultant flow of the inflow normal to the disk is then computed. The normal flow is assumed to be present on the propeller, but in a direction opposite to the tilted lift vector. In this manner, the He-Peters model gives the exact normal flow and swirl velocity on the propeller for an infinite number of blades.

However, when one computes the change in this velocity due to the finite number of blades (losses near the root and tip), one finds that the He-Peters model over-predicts the amount of higher-harmonic induced flow at non-zero multiples of the number of blades. To correct for this, the present paper proposes the addition of extra mass terms into the He-Peters model. These additional mass terms model the extra kinetic energy in swirl modes as compared to axial flow inflow modes. We will show how the added mass leads to good agreement for the velocity field.

A unique opportunity to study propeller aerodynamics exists by comparison with the exact solutions by Prandtl and Goldstein. Coupled system effects are not included, such as those due to blade dynamics, airfoil lift characteristics, a root cutout or an engine nacell. These effects would likely be inherent in any experimental design. The physical phenomena described by the exact solutions would also be present in physical experiments, but may be difficult to observe due to the design limitations. The solution space of the dynamic wake model can be improved by comparison with these exact solutions, which describe a particular aerodynamic phenomena in isolation from other physical effects.

The original question of the research project was to determine if the dynamic wake model could accurately reproduce the results of solutions by Goldstein and Prandtl. The dynamic wake model should agree with these solutions when applied to the same idealized system. Poor correlation is an illustration of a fundamental error in the derivation of the dynamic wake model. Strong correlation with the original He-Peters dynamic wake model was observed for large tip-speed ratios ($\mu_0 \geq 20$). Poor correlation for smaller tip-speed ratios was hypothesized to be due to the neglect of the in-plane mass component. The mass matrix of the He-Peters dynamic wake model was modified to include this physical effect present at smaller tip-speed ratios ($\mu_0 < 20$). An explanation of the physical phenomenon will be given along with the corresponding mathematical derivation to modify the mass matrix. The new mass matrix can then be substituted into the dynamic wake model. The calculation equations will then be derived.

Adapting Dynamic Wake Models to Propeller Dynamics The dynamic wake model was originally designed for helicopter rotors in axial and skewed flow. The properties of the model's actuator disk lend themselves well to approximating the aerodynamics of typical helicopter advance ratios in skewed flow and inflow ratios in axial flow. The dynamic wake model is only capable of modelling vertically directed thrust vectors (Fig 3) which is a consequence of the discontinuity of ν across the actuator disk, $\eta = 0$, for the ellipsoidal coordinate system.

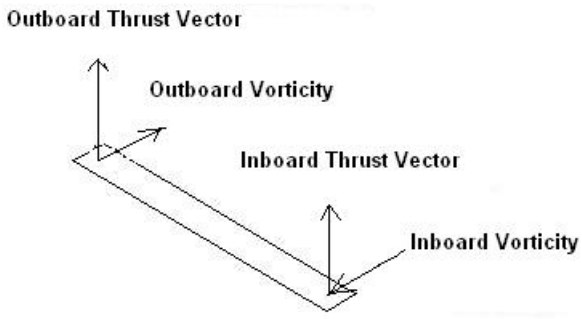

Figure 3: Dynamic wake model approximation for thrust and vorticity vectors.

Actual thrust vectors (Fig 4) are slightly tilted off the vertical ($2^0 \leq \phi \leq 14^0$) at the blade-tip and horizontally directed at the blade root ($\phi = 90^0$). Figure 5 shows the tilt-angle profile for slow and fast inflow ratios, $\varphi = \arctan(1/\mu)$. The tilt-angle is low for a slow inflow ratio ($\lambda = 0.05$, $\mu_0 = 20$)

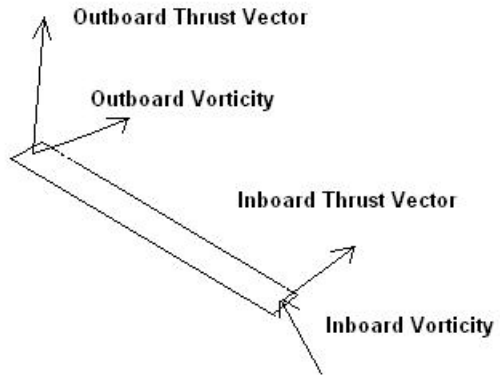

Figure 4: Thrust and vorticity vectors for a real propeller blade.

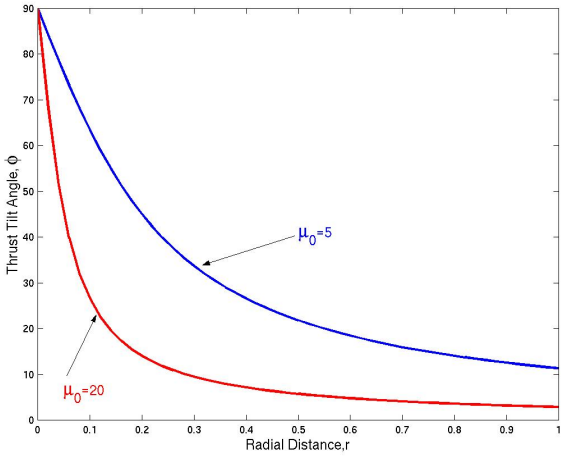

Figure 5: Tilt angle, off the vertical, for the thrust vector along propeller blade for tip speed ratios, μ_0, of 5 and 20.

while the tilt-angle for a fast inflow ratio is significantly greater ($\lambda = 0.2, \mu_0 = 5$).

Approximating the thrust vectors with vertical components only is a more reasonable approximation for low thrust tilt-angle, $\mu_0 = 20$, but not for a high tilt-angle profile ($\mu_0 = 5$). The vortex sheet helix (Fig 1) extends along the longitudinal axis as the thrust tilt-angle changes from low to high profile. A constant horizontal profile for the vorticity vectors becomes a worse approximation as the trailing vortex helix is extended. The approach of the dynamic wake model implies flat horizontal vortex sheets that translate downstream at the induced velocity, w (Fig 6). The modelling approximation neglects the angle that vorticities shed off the blade, which is the same as the thrust-tilt angle, ϕ. The important physical phenomena for small tip-speed ratios ($\mu_0 = 5$) that was missing from the original He-Peters model was the effect of the swirl velocity for finite number of blades. The He-Peters model correctly predicts the swirl velocity for the infinite blade case (Ref 2), but not the finite blade case. The wake spacing is classically defined as the vertical distance between consecutive vortex sheets at the sheets' edges (Ref 4). The azimuthally curved distance that intersects the sheets normally, or the *normal wake spacing*, is a physically more reasonable parameter. Near the root of the vortex helix this becomes more important for small tip-speed ratios. The normal wake spacing near the root can be described as $2\pi\bar{r}/Q$, which is independent of the tip-speed ratio. On the contrary, the vertical wake spacing at the sheets' edges is $s = 2\pi/(Q\mu_0)$. The normal distance between the sheets near the helix root needs to be taken into account.

A new mass matrix is formed by including a weighting function to account for the mass correction factor near the root. The mass correction factor accounts for the nonzero normal wake spacing due to a finite number of blades, and is associated with the test functions. The expansion series of trial functions remains the same. The weighting function is analogous to a transformation between coordinate systems. The transformation in this case is to represent the actual induced velocity and wake spacing, normal to the vortex sheets at some shed angle (Fig 7) in the dynamic wake model, which has flat horizontal vortex sheets (Fig 6). The methodology for using the dynamic wake model remains the same. An additional component is that the wake model must take the transformation of the normal local wake spacing into account, which is now included with the new formulation. Thus, after adding the extra mass, one applies the He-Peters model as it has been applied in the past.

1. Calculate the magnitude of the tilted lift vector.

2. Substitute the lift magnitude into the vertical component within the dynamic wake model.

3. Calculate the induced velocity with the dynamic wake model, which will only consist of a vertical component.

4. Substitute this induced velocity magnitude into the coupled model, in the opposite direction to the lift.

Mathematical Formulation

The dynamic wake model is an expansion of the momentum equation, in a non-dimensional linearized form, equation (1).

$$\frac{\partial \vec{v}}{\partial \tau} - v_\infty \frac{\partial \vec{v}}{\partial \xi} = -\vec{\nabla} p \tag{1}$$

The similarity between the momentum equation and the dynamic wake model, equation (2), can be seen. The dynamic wake model is presented in the axial flow form.

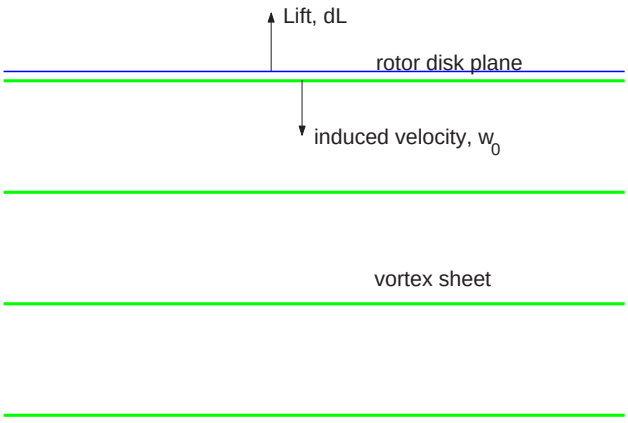

Figure 6: Dynamic wake model approximation for the thrust and induced velocity vectors

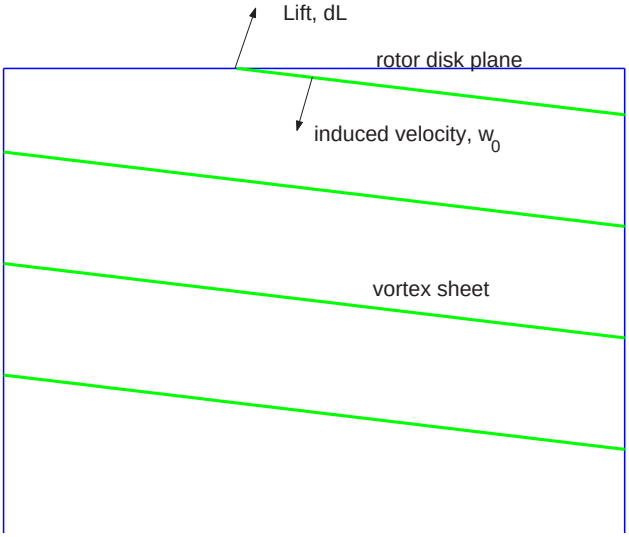

Figure 7: Thrust and induced velocity vectors for actual trailing vortex

(2)
$$\begin{bmatrix} [K_n^m] & 0 \\ 0 & [K_n^m] \end{bmatrix} \begin{Bmatrix} \frac{\partial \alpha_n^m}{\partial \tau} \\ \frac{\partial \beta_n^m}{\partial \tau} \end{Bmatrix} + \begin{bmatrix} [B_{jn}^m] & 0 \\ 0 & [B_{jn}^m] \end{bmatrix} \begin{Bmatrix} \alpha_n^m \\ \beta_n^m \end{Bmatrix} = \begin{Bmatrix} \tau_n^{mc} \\ \tau_n^{ms} \end{Bmatrix}$$
$$m \in \{0,1,2,3,\ldots\}$$
$$n \in \{m+1, m+3, m+5, \ldots, N_m\}$$

A change of variable can be done to change from a non-rotating, equation (2), to a rotating coordinate system, equation (3). The resulting equation is shown with time derivatives set to zero since there will be no transient changes in lift on the blade in the rotating system. The portion of the time-derivative in the non-rotating system due to periodic passing of the blades is embedded in this steady-equation, equation (3), as the term $m\mu_0[K_n^m]$.

(3)
$$\begin{bmatrix} [B_{jn}^m] & -m\mu_0[K_n^m] \\ m\mu_0[K_n^m] & [B_{jn}^m] \end{bmatrix} \begin{Bmatrix} \hat{\alpha}_n^m \\ \hat{\beta}_n^m \end{Bmatrix} = \frac{\mu_0}{2} \begin{Bmatrix} \hat{\tau}_n^{mc} \\ \hat{\tau}_n^{ms} \end{Bmatrix}$$

For the infinite blade case, the only order index included is $m = 0$. The mass matrix, multiplied by index m, does not enter into this calculation. The original dynamic wake model correctly predicts the inflow to pressure relationship for the infinite-blade case. The poor prediction for the finite-blade case is due to physical phenomena not accounted for in the mass matrix of the original model.

Mass Matrix Calculation The original and new mass matrices will be compared before further derivation with the dynamic wake model. The original mass matrix calculation was formed from transformation of the velocity expansion series to a discrete domain by utilizing the same test functions as the trial functions. The result is presented as equation (4).

(4)
$$[K_n^m] = K_n^m \int_{\nu=0}^{1} \bar{P}_j^m(\nu)\bar{P}_n^m(\nu)d\nu = K_n^m \delta_{jn}$$
$$(m+n) \in O \quad (m+j) \in O$$

The modified mass matrix has a weighting function to account for the normal wake spacing and to reflect the nonzero mass at the root, equation (5).

(5)
$$[M_{jn}^m] = K_n^m \int_{\nu=0}^{1} (1 + m(\frac{k}{Q\mu_0})^2 \frac{1}{\bar{r}^{2m}}) \bar{P}_j^m(\nu)\bar{P}_n^m(\nu)d\nu$$

The normal wake spacing is accounted for in the weighting function by the factor $m(k/(Q\mu_0))^2$, and the finite mass at the root is accounted for by the factor $1/\bar{r}^{2m}$. The expression inside the integral can be manipulated in the following manner, equation (6).

$$(6)\quad [M_{jn}^m] = K_n^m \int_{\nu=0}^{1} \bar{P}_j^m(\nu)\bar{P}_n^m(\nu)d\nu + mK_n^m\left(\frac{k}{Q\mu_0}\right)^2 \int_{\nu=0}^{1} \frac{\bar{P}_j^m(\nu)\bar{P}_n^m(\nu)}{(1-\nu^2)^m}d\nu$$

This form contains the original orthogonality integral, (4), and another integral weighted inversely by $\bar{r}^2 = 1-\nu^2$. It can be shown (Ref 12) that equation (6) can be represented in closed form as equation (7).

$$(7)\qquad [M_{jn}^m] = [K_n^m]\left([I] + m\left(\frac{k}{Q\mu_0}\right)^2[[I] - [A_{jn}^m]^2]^{-m}\right)$$

The empirical factor, k, scales the weighting function, and remains to be chosen. The optimal k-value depends upon the exact solution used for comparison. The k-value for convergence to the Goldstein solution will be different than the k-value used to converge to the Prandtl solution. Several other variations of the weighting function were attempted, but the best results were obtained were obtained from the form presented above.

He-Peters Inflow Solution We begin with the He-Peters dynamic wake model for axial flow in a rotating coordinate system, with the modified mass matrix, $[M_{jn}^m]$, substituted in for the original matrix, $[K_n^m]$. The same derivation can be done with the original K_n^m-matrix for calculations with the original model formulation. Equation (3) is true for all orders m, and all degrees, n, where $n+m \in O$. The number of degree terms, N_m, for each order m can be arbitrarily chosen since each order expansion is uncoupled for axial flow. The sine-component pressure coefficients, $\hat{\tau}_n^{ms}$, are also zero since $\sin(m\hat{\psi})$ is an odd function and the pressure field over the disk will be modelled as an even function. Separate the matrix equation according to the sine and cosine components of the pressure field, equations (8) and (9).

$$(8)\qquad [B_{jn}^m]\{\hat{\alpha}_n^m\} - m\mu_0[M_{jn}^m]\{\hat{\beta}_n^m\} = \frac{\mu_0}{2}\{\hat{\tau}_n^{mc}\}$$

$$(9)\qquad \{\hat{\beta}_n^m\} = -m\mu_0[B_{jn}^m]^{-1}[M_{jn}^m]\{\hat{\alpha}_n^m\}$$

Combine the cosine and sine components, equations (8) and (9), by substitution and solve for $\{\hat{\alpha}_n^m\}$, equation (10).

$$(10)\quad \{\hat{\alpha}_n^m\} = [[B_{jn}^m] + m^2\mu_0^2[M_{jn}^m][B_{jn}^m]^{-1}[M_{jn}^m]]^{-1}\frac{\mu_0}{2}\{\hat{\tau}_n^{mc}\}$$

Note that for the zeroth order (m=0), the relationship between the coefficients for velocity field and pressure field expansions simplifies to equation (11) since $[A_{jn}^0] = [B_{jn}^0]^{-1}$.

$$(11)\qquad \{\hat{\alpha}_n^0\} = \frac{\mu_0}{2}[A_{jn}^0]\{\hat{\tau}_n^{0c}\}$$

Vortex Line Circulation Replacing the propeller blade with a vortex line, as done in classic solutions (Ref 4, 6) implies Dirac's delta lifting function on the azimuthal coordinate, $\delta(\hat{\psi}-\psi_q)$ at the half-chord. The pressure field input into the dynamic wake model will be generated from Kutta's formula (Ref 1) applied to a propeller, equation (12), a Legendre series expansion of the circulation function, equation (13), and the transform between the lift profile and pressure field expansion coefficient, equations (14) and (15). The pressure field coefficient formulas have already been derived assuming Dirac's delta as the chordwise lift distribution.

$$(12)\qquad \bar{\Gamma} = \frac{QL\mu_0}{2\pi\bar{r}}\frac{\mu}{\sqrt{1+\mu^2}}$$

$$(13)\qquad \bar{\Gamma} = \frac{\mu}{\sqrt{1+\mu^2}}\sum_{j=1}^{J}\gamma_j\bar{P}_j^0(\nu)$$

$$(14)\qquad \hat{\tau}_n^{0c} = \frac{Q}{2\pi}\int_0^1 \frac{L}{\bar{r}}\bar{P}_n^0(\nu)d\nu$$

$$(15)\qquad \hat{\tau}_n^{mc} = \frac{Q}{\pi}\int_0^1 \frac{L}{\bar{r}}\bar{P}_n^m(\nu)d\nu$$

Lift can be described in terms of non-dimensional circulation, equation (12), around the propeller blade at some radius, $\bar{r}$, for a tip-speed ratio, μ_0. The order index of the pressure coefficients $(\hat{\tau}_n^{mc}, \hat{\tau}_n^{ms})$ is only indexed to multiples of the number of blades, Q, instead of all integers. The order index subset $m \in \{0, Q, 2Q, \ldots\}$ is a consequence of the derivation for calculating coefficients from the original pressure expansion series (Ref 12). Pressure coefficients for $m \notin \{Q, 2Q, 3Q, \ldots\}$ are zero. The velocity coefficients $(\hat{\alpha}_n^m, \hat{\beta}_n^m)$ for the same order indexes are also correspondingly zero. The sine component $\hat{\tau}_n^{ms}$ is also zero because the chordwise lift distribution will be modelled as an even function, whereas $\sin(m\bar{\psi})$ is an odd function.

The formulas for $\hat{\tau}_n^{0c}$ and $\hat{\tau}_n^{mc}$ are multiplied by μ_0 and the circulation to lift relationship, equation (12), is then substituted into both pressure expansion transforms, equations (14) and (15), to obtain equations (16) and (17).

$$(16)\qquad \mu_0\hat{\tau}_n^{0c} = \int_0^1 \bar{\Gamma}\frac{\sqrt{1+\mu^2}}{\mu}\bar{P}_n^0(\nu)d\nu$$

$$\mu_0 \hat{\tau}_n^{mc} = 2 \int_0^1 \bar{\Gamma} \frac{\sqrt{1+\mu^2}}{\mu} \bar{P}_n^m(\nu) d\nu \tag{17}$$

Next, substitute in the circulation expansion series, equation (13) to obtain equations (18) and (19).

$$\mu_0 \hat{\tau}_n^{0c} = \sum_{j=1}^{J} \gamma_j \int_0^1 \bar{P}_j^0(\nu) \bar{P}_n^0(\nu) d\nu \tag{18}$$

$$\mu_0 \hat{\tau}_n^{mc} = 2 \sum_{j=1}^{J} \gamma_j \int_0^1 \bar{P}_j^0(\nu) \bar{P}_n^m(\nu) d\nu \tag{19}$$

The integral of the Legendre expansion series can be expressed in terms of the inner product of two vectors, equations (20) and (21). The vector relationship is used to construct the matrix multiplication for the transform between the domain of the vectors of $\{\gamma_j\} = \begin{Bmatrix} \gamma_1 & \gamma_3 & \gamma_5 & \dots \end{Bmatrix}^T$ and $\{\hat{\tau}_n^{mc}\} = \begin{Bmatrix} \hat{\tau}_{m+1}^{mc} & \hat{\tau}_{m+3}^{mc} & \hat{\tau}_{m+5}^{mc} & \dots \end{Bmatrix}^T$.

$$\mu_0 \hat{\tau}_n^{0c} = \{ \int_0^1 \bar{P}_j^0(\nu) \bar{P}_n^0(\nu) d\nu \}^T \{\gamma_j\} \tag{20}$$

$$\mu_0 \hat{\tau}_n^{mc} = 2\{ \int_0^1 \bar{P}_j^0(\nu) \bar{P}_n^m(\nu) d\nu \}^T \{\gamma_j\} \tag{21}$$

The expansion transformation matrix is now defined, equation (22).

$$E_{jn}^{m0} = \int_0^1 \bar{P}_j^0(\nu) \bar{P}_n^m(\nu) d\nu \tag{22}$$

Equations (23) and (24) describe the pressure field coefficients, equations (14) and (15), in terms of the circulation expansion coefficients, equation (13), and the transformation matrix, equation (22).

$$\mu_0 \{\hat{\tau}_n^{0c}\} = [E_{jn}^{00}] \{\gamma_j\} \tag{23}$$

$$\mu_0 \{\hat{\tau}_n^{mc}\} = 2[E_{jn}^{m0}] \{\gamma_j\} \tag{24}$$

Inflow Distribution The velocity field expansion in the rotating coordinate system, equation (25), is shown below, where N_m specifies the highest degree for the expansion of order m.

$$w_0(\bar{r}, \hat{\psi}) = \sum_{m=0}^{m_{max}} \sum_{n=m+1}^{\mathcal{N}_m} \frac{1}{\nu} \bar{P}_n^m(\nu) [\hat{\alpha}_n^m \cos(m\hat{\psi}) + \hat{\beta}_n^m \sin(m\hat{\psi})] \tag{25}$$

The azimuthal angle, $\hat{\psi}$, can be set to any of the various blade angles, $\hat{\psi} = \psi_q$ for $q \in \{1, 2, \dots, Q\}$. The possible values of ψ_q for a two-bladed propeller are $\{\psi_1, \psi_2\} = \{0, \pi\}$, and the possible values of ψ_q for a four-bladed propeller are $\{\psi_1, \psi_2 \psi_3, \psi_4\} = \{0, \frac{\pi}{2}, \pi, \frac{3\pi}{2}\}$. The expansion simplifies to equation (26) on the reference blade, $\hat{\psi} = \psi_1 = 0$.

$$w_0(\bar{r}, \psi_q) = \sum_{m=0}^{m_{max}} \sum_{n=m+1}^{\mathcal{N}_m} \frac{1}{\nu} \bar{P}_n^m(\nu) \hat{\alpha}_n^m \tag{26}$$

The optimal induced velocity in the far wake on the vortex sheet, w_B, is the Betz distribution (Ref 4) and can be expanded with zeroth order shape functions, $\bar{P}_n^0/\nu$, used for the velocity expansion, equation (26).

$$w_B(\bar{r}) = \frac{\mu}{\sqrt{1+\mu^2}} = \sum_{j=1}^{J} \lambda_j \frac{1}{\nu} \bar{P}_j^0(\nu) \tag{27}$$

The orthogonality property of Legendre functions is used to manipulate equation (27) and form the λ-vector definition, equation (28).

$$\lambda_j \equiv \int_0^1 \frac{\mu}{\sqrt{1+\mu^2}} \bar{P}_j^0(\nu) \nu d\nu \tag{28}$$

The velocity at the propeller reference blade, (26), is half the Betz velocity, equation (27), at the corresponding vortex sheet in the far wake, equation (29).

$$\frac{1}{2} \frac{\mu}{\sqrt{1+\mu^2}} = \sum_{m=0}^{m_{max}} \sum_{n=m+1}^{\mathcal{N}_m} \frac{1}{\nu} \bar{P}_n^m(\nu) \hat{\alpha}_n^m \tag{29}$$

The relationship between velocity fields at the disk and in the far wake, equation (29), can be transformed to a discrete domain by utilizing the orthogonality property used to derive equation (28).

$$\frac{1}{2} \int_0^1 \frac{\mu}{\sqrt{1+\mu^2}} \bar{P}_j^0(\nu) \nu d\nu = \sum_{m=0}^{m_{max}} \sum_{n=m+1}^{\mathcal{N}_m} \hat{\alpha}_n^m \int_0^1 \bar{P}_j^0(\nu) \bar{P}_n^m(\nu) d\nu \tag{30}$$

The expansion for velocity in the far wake is now described as a sum of inner products, where the summation index is the Legendre function order, equation (31).

$$\frac{1}{2}\lambda_j = \sum_{m=0,Q,2Q,\ldots}^{m_{max}} \left\{ \int_0^1 \bar{P}_j^0(\nu)\bar{P}_n^m(\nu)d\nu \right\}^T \{\hat{\alpha}_n^m\} \tag{31}$$

The integral in equation (31) is the transpose of the expansion transformation matrix, equation (22). Equation (31) can compactly represented as a matrix relationship where $[E_{jn}^{m0}]$ in the $m = 0$ term is the identity matrix, equation (32).

$$\frac{1}{2}\{\lambda_j\} = \{\hat{\alpha}_n^0\} + \sum_{m=Q,2Q,\ldots}^{m_{max}} [E_{jn}^{m0}]^T \{\hat{\alpha}_n^m\} \tag{32}$$

Combining Circulation, Inflow and the Dynamic Wake Model The final calculation equation for the infinite-blade case is formed by combining equations (11), (23) and (32). The infinite-blade case consists of only zeroth order terms, $m = 0$, so the summation of $m \geq 0$ terms in equation (32) is neglected. The resulting equation for the infinite-blade case is equation (33).

$$\{\lambda_j\} = [A_{jn}^0]\{\gamma_j\} \tag{33}$$

The final calculation equation for the finite-blade case is formed by combining equations (11), (10), (23), (24) and (32). The result is presented as equation (34) and relates the Betz velocity far downstream of the propeller, $\{\lambda_j\}$, to the circulation at the propeller blades, $\{\gamma_j\}$.

$$\{\lambda_j\} = [A_{jn}^0]\{\gamma_j\} + \left[2 \sum_{m=Q,2Q,\ldots}^{m_{max}} [E_{jn}^{m0}]^T [[B_{jn}^m] + m^2\mu_0^2 [M_{jn}^m][A_{jn}^m][M_{jn}^m]]^{-1} [E_{jn}^{m0}] \right] \{\gamma_j\} \tag{34}$$

The vector $\{\lambda_j\}$ is numerically calculated with equation (28). The matrices in each term in equation (34) can be added together and the resulting matrix can then be inverted to calculate the circulation coefficients, γ_j. The calculated circulation can then be plotted with equation (13).

Exact Solutions and Relative Error Golstein's solution is presented for a Q-bladed system (35). The derivation of this is presented in Goldstein's original publication (Ref 6). The function $T_{\kappa,\zeta}$ is the real finite portion of the Lommel function $S_{\kappa,\zeta}$, which is a particular solution to Bessel's equation (Ref 6), (Ref 10, p.937, Equation 8.577).

$$\bar{\Gamma}_g(\mu) = \frac{8}{\pi^2} \sum_{m=0}^{\infty} \frac{T_{1,Q(m+\frac{1}{2})}[Q(m+\frac{1}{2})\mu]}{(2m+1)^2} + \frac{2}{\pi} \sum_{m=0}^{\infty} a_m \frac{I_{Q(m+\frac{1}{2})}[Q(m+\frac{1}{2})\mu]}{I_{Q(m+\frac{1}{2})}[Q(m+\frac{1}{2})\mu_0]} \tag{35}$$

The coefficients in Goldstein's solution must be solved for numerically. The following matrix relationship, equation (36), is derived by Goldstein and shown again by Makinen (Ref 12). Numerical calculation of Goldstein's solution requires representing the function $T_{1,Q(m+\frac{1}{2})}$. Derivation of a sin series to represent this function will be shown by Makinen (Ref 12). The argument of I, I', T and T' is $Q(m+\frac{1}{2})\mu_0$ and the argument of K and K' is $Qn\mu_0$.

$$\sum_{m=0}^{\infty} \frac{a_m}{4n^2-(2m+1)^2} \left[(2m+1)\frac{I'_{Q(m+1/2)}}{I_{Q(m+\frac{1}{2})}} - 2n\frac{K'_{Qn}}{K_{Qn}} \right] = \frac{4}{\pi} \sum_{m=0}^{\infty} \frac{1}{4n^2-(2m+1)^2} \frac{1}{(2m+1)^2} \times \left[2n\frac{K'_{Qn}}{K_{Qn}} T_{1,Q(m+\frac{1}{2})} - (2m+1)T'_{1,Q(m+\frac{1}{2})} \right] \quad \text{for } n \in \{1,2,3,\ldots\} \tag{36}$$

Prandtl's solution, equation (37), will also be used for comparison in the results section. The decay multiplier, $\arccos(e^{\frac{-Qf}{2}})$, operates analogously to the modified Bessel functions of the first kind, $I_{Q(m+\frac{1}{2})}$, in Goldstein's solution.

$$\bar{\Gamma}_p(\mu) = \frac{2}{\pi}\frac{\mu^2}{1+\mu^2}\arccos(e^{\frac{-Qf}{2}}) \quad f = (1-\frac{\mu}{\mu_0})\sqrt{1+\mu_0} \tag{37}$$

All finite-blade circulation solutions go to zero at the blade-tip. Goldstein's solution, equation (35), only goes to zero if the summation series is evaluated with an infinite number of terms. The series converges slowly, so a significant discontinuity will be present at the blade tip for a truncated series. To account for this, a modified form of Goldstein's solution is presented, equation (38).

$$\bar{\Gamma}_{gm}(\mu) = \bar{\Gamma}_g(\mu) + \bar{\Gamma}_g(\mu_0)\arccos(e^{\frac{-Qf}{2}}) \quad f = (1-\frac{\mu}{\mu_0})\sqrt{1+\mu_0} \tag{38}$$

The results section will show results of both the modified and unmodified forms of Goldstein's solution. The modified solution form can be more useful for computer calculations by avoiding anomalies that would be due to the non-physical blade-tip discontinuity.

$$e_\nu = \frac{\int_{\nu=0}^{1} (F_{ex} - F_{app})^2 d\nu}{\int_{\nu=0}^{1} F_{ex}^2 d\nu} \times 100\% \tag{39}$$

The relative error norm for comparison of the He-Peters approximate and Prandtl's exact circulation solutions will be calculated with equation (39).

Results

The results of the above mathematical formulation will be presented here. A comparison of the exact solution is shown to illustrate the modelling differences. Several cases will also be compared with results from the He-Peters model to illustrate the success of the new formulation. Error Norms will then be presented to quantitatively illustrate the advantage of the new model formulation. All calculations were done with Matlab 5.0 with the default double precision accuracy. Calculations with the He-Peters model were done with the order index, m, being indexed up to a maximum, $m_{max} = 20$, except for $Q = 3$ cases where $m_{max} = 21$. The number of terms for each order expansion is $N_m = 11$. The expansion conversion matrix $[E_{nj}^{m0}]$ and vector $\{\lambda_j\}$ and relative error norms were calculated numerically with a variable step size trapezoidal integration algorithm to an absolute tolerance less than 0.001 for the entire integration range $\nu \in [0,1]$. All other matrices can be calculated from closed form solutions (Ref 9). Most calculations with the Goldstein solution had 50 terms. The empirical factor for the modified He-Peters model was chosen to be $k = 2.2$. This value was chosen for best convergence to Prandtl's solution from error norm surface plots with independent variables k and μ_0 (Ref 12). Matlab frequently showed warnings about a possible matrix conditioning problem during calculations with the modified mass matrix. However, no results were obtained to suggest that the condition of this matrix affects the numerical solution adversely.

The results in figure 8 is an attempt to reproduce the plot (Ref 6, p.456, Fig 2) presented by Goldstein to compare his solution with that of Prandtl for $Q = 2$, $\mu_0 = 5$. The infinite blade case is also presented to illustrate how Prandlt's solution converges to the infinite blade solution at the inboard region. Three versions of Goldstein's solution are presented to illustrate ways of accounting for the summation series truncation. The twenty- and fifty-term Goldstein solutions illustrate that the blade-tip discontinuity converges to zero slowly. The modified form of Goldstein's solution does not have this discontinuity and can be successfully used in further computer calculations without introducing numerical anomalies. Close analysis of the Goldstein solutions shows that the modified solution and the original fifty-term solution diverge from the original twenty-term solution at the same location. The similar divergence of the original and modified fifty-term solutions shows that the correction decay factor

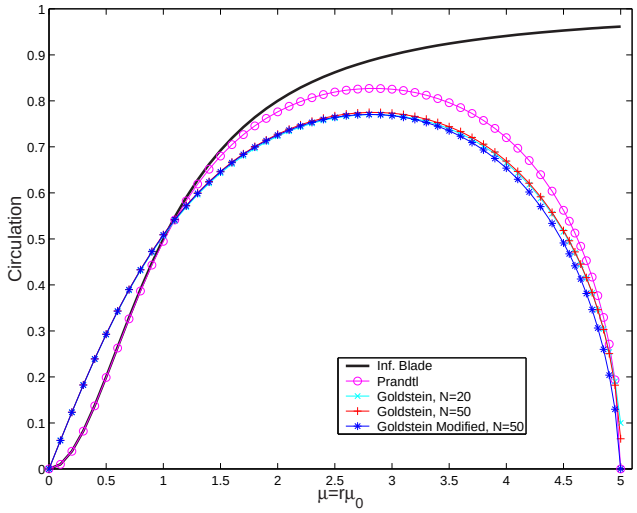

Figure 8: Exact solutions for infinite and finite blade cases. The two dimensional solution is by Prandtl and the three dimensional solution is by Goldstein. The modified Goldstein solution is introduced to account for the blade-tip discontinuity due to truncation of the solution series.

does not introduce anomalies at the inboard or medial regions. The decay correction factor acts in an analogous manner to the modified Bessel functions of the first kind, $I[Q(\frac{1}{2}+m)\mu]$. An important physical difference between the solutions by Prandtl and Goldstein is the behavior at the far inboard region. The Goldstein solution overshoots that of Prandtl and the infinite blade solution, near the root, which reflects important behavior of the trailing vortex.

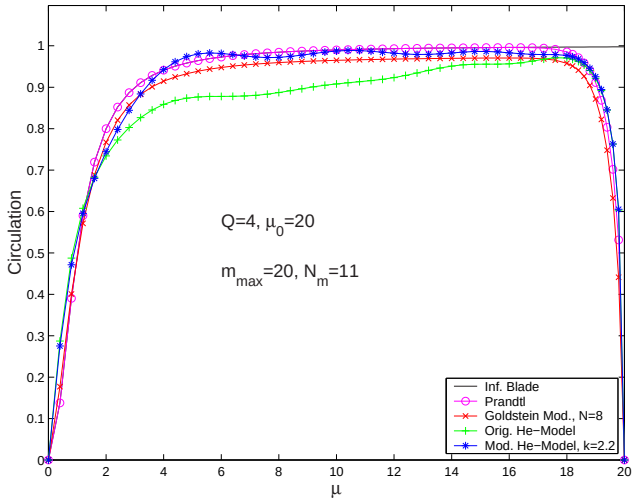

Figure 9: Comparison of original and modified forms of the He-Peters model are compared for conditions within the applicable range of the original model, tip-speed ratio $\mu_0 = 20$ and number of blades $Q = 4$.

The original and new form of the He-Peters model are compared in figure 9 for flight conditions within the range

for which the original model is a reasonable approximation ($\mu_0 = 20$, $Q = 4$). The modified He-Peters model converges to the exact solution better than does the original formulation, even though this flight condition was considered within the applicable range of the original formulation. The original model converges to the exact solution at the outboard region, but not at the inboard region. The divergence is due to the modelling error at the blade root. Prandtl and Goldstein solutions are similar for this flight condition, the modelling errors of a two-dimensional solution become more prominent for larger wake spacing.

Interestingly, the Prandtl and Goldstein solutions converge near the root, and the He-Peters model solution overshoots the exact solutions, which is characteristic of this case only. The Goldstein solution overshoots all other solutions at the root for cases with smaller tip-speed ratios and fewer blades. The Goldstein solution was only presented with eight terms due to a numerical accuracy problem in the Goldstein coefficient matrix, equation (36), which will be discussed later.

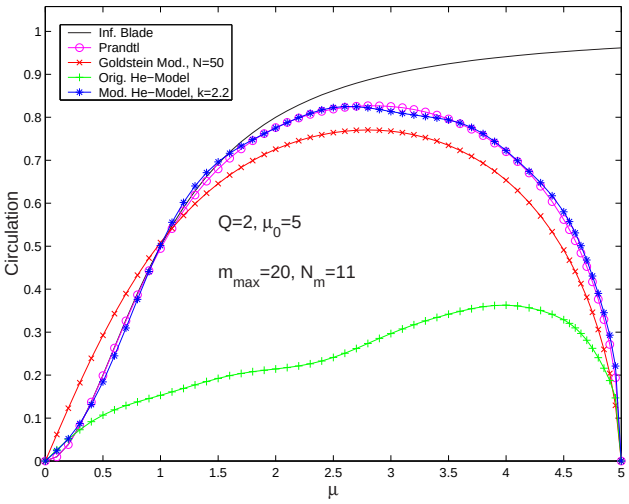

Figure 10: Comparison of original and modified forms of the He-Peters model are compared for conditions outside of the applicable range of the original model, tip-speed ratio $\mu_0 = 5$ and number of blades $Q = 2$.

In figure 10, the solutions are compared for a two-bladed propeller at a tip-speed ratio of $\mu_0 = 5$, which is far outside of the acceptable conditions for the original dynamic wake model formulation. The original He-Peters model solution is suppressed far below the exact solutions and is not physically meaningful at all. The modified dynamic wake model shows a clear convergence to Prandtl's solution. An important characteristic of the solutions at the blade root becomes prominent for large wake spacing cases, such as this example. In particular, the Goldstein solution approaches zero with a non-zero slope. The profile of the modified He-Peters model clearly converges to Prandtl solution. A different k-value could be chosen to cause the modified He-Peters model to converge to the Goldstein solution, but this would only cause convergence at the medial and outboard blade regions. The modes included in the He-Peters dynamic wake model have a zero slope at the blade root ($\bar{r} = 0$). The Goldstein model has a non-zero slope at the blade root thus convergence cannot occur there. The current formulation does model the root of the disk with nonzero mass flow, but the slope of the mode shapes is still zero at center of the disk.

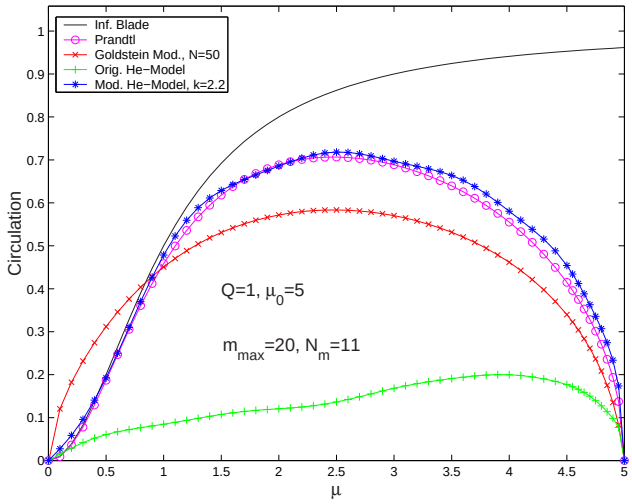

Figure 11: An illustration to show that the new model formulation can be extrapolated to a single-blade propeller, tip-speed ratio $\mu_0 = 5$ and number of blades $Q = 1$.

The dynamic wake model was also used to calculate the results for a single-bladed propeller at tip-speed ratio $\mu_0 = 5$ (Fig 11). The new He-Peters formulation clearly captures the essence of the physics more than the original formulation. The original formulation results are suppressed far below the exact solutions. The new formulation converges the the Prandtl solution once again for the same empirical value, $k = 2.2$. The profile for Goldstein's solution diverges from Prandtl's solution even more significantly than for the case $Q = 2$, $\mu_0 = 5$ because the wake spacing for a single-bladed propeller is twice that of a two-bladed propeller. The inboard behavior of Goldstein's solution is also more prominent for this case, emphasizing the need to model behavior of the blade root properly for small tip-speed ratios, $\mu_0 \leq 5$.

Figure 12 shows results from the dynamic wake model for a case outside of the applicable range of the new formulation ($Q = 2$, $\mu_0 = 2$). The wake spacing for this case is also too large for the applicable range of Prandtl's solution (Ref 11) but the purpose here is to illustrate the mathematical nature of the divergence from Prandtl's solution. The two-dimensional exact solution decays below the infinite-blade case at the inboard region ($\mu \approx 0.4$). The modified He-Peters solution remains converged to the infinite-blade solution at the inboard and medial blade regions. The weighting function in

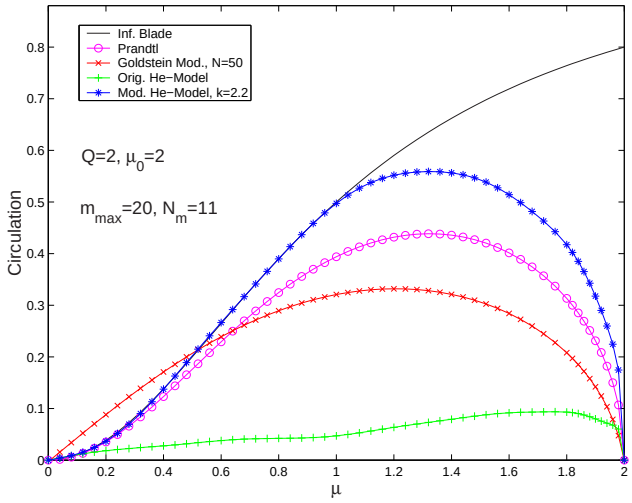

Figure 12: An attempt to predict the circulation with the new model formulation for tip-speed ratio, $\mu_0 = 2$, outside of the applicable range, number of blades $Q = 2$.

the modified He-Peters model, $(1+m(k/(Q\mu_0))^2)/\bar{r}^{2m}$, does not shift the mass inboard enough for this case. The modified Goldstein curve represents the correct physical solution. The original He-Peters solution is suppressed far below the exact solution and is not physically representative.

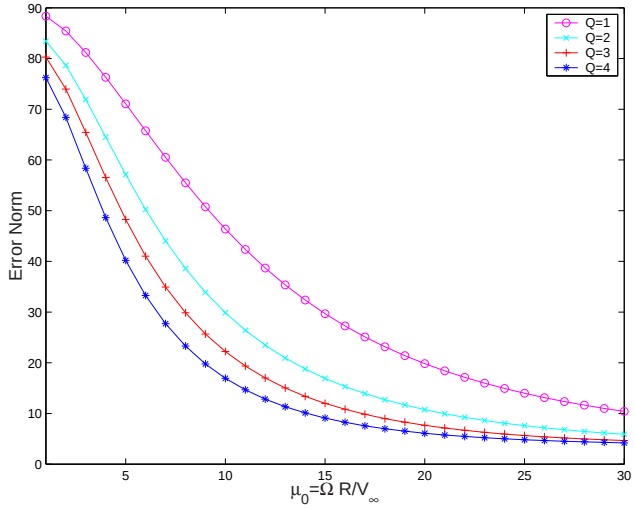

Figure 13: Relative error norm for the original He-Peters model for tip-speed ratios $1 \leq \mu_0 \leq 30$ for number of blades $Q = 1,2,3,4$.

Relative error norms for the original He-Peters dynamic wake model, relative to the Prandtl solution, were calculated, equation (39). The percent error decreases for increasing number of blades, but the large error profile shows that the original model does not capture the physical phenomena. The error for tip-speed ratio $\mu_0 = 30$ ranges from approximately 4 to 10%. The four-bladed case increases to over 10% error at a tip-speed ratio $\mu_0 = 15$. Only one error norm for the original He-Peters model was compared to the new formulation error norms because only a qualitative comparison is needed to show the success of the new formulation.

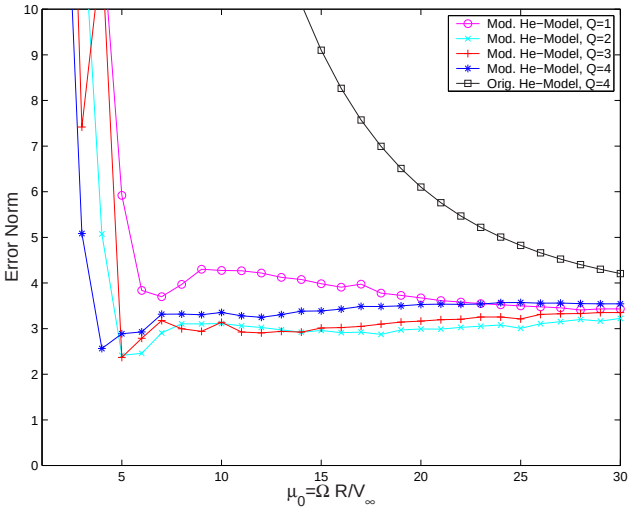

Figure 14: Relative error norm for the modified formulation of the He-Peters model for tip-speed ratios $1 \leq \mu_0 \leq 30$ for number of blades $Q = 1,2,3,4$. The four-blade error norm for the original He-Peters model is included to illustrate the qualitative comparison.

The error norms for the new formulation are relatively constant at 3% for tip-speed ratios $\mu_0 \geq 5$ (Fig 14). The modelling approach breaks down at a discrete lower bound ($4 \leq \mu_0 \leq 6$) depending on the number of blades, Q. The results for the four-bladed propeller with original model formulation are also presented to illustrate the large qualitative difference between new and original formulations.

An anomaly for the three-bladed case is also present. The error norm for $Q = 3$ has a spike at $\mu_0 = 4$, but the functional is known to be smooth, equation (39). Similar anomalies were observed in other error norm calculations. The other anomalies appeared when calculation programs were called within for-loops to repetitiously calculate the error norm for numerous values of k and μ_0. Non-anomalous error norm values resulted when the programs were set up to calculate specifically at at the k-μ_0-value where the anomaly originally occurred. The anomaly shown above ($Q = 3$, $\mu_0 = 4$, $k = 2.2$) could not be resolved, however it is thought to be due to software problems and not physically or mathematically representative of the dynamic wake model or the exact solutions.

Summary and Conclusions

The applicable range of the dynamic wake model for axial flow is greatly expanded with the new formulation, which can be applied by a simply substituting the new mass matrix for the original mass matrix, equations (4) and (7). The

new mass matrix approximates the nonzero mass at the blade root as a function of radius. The current form of the dynamic wake model with Legendre function modes ($m \in \{0, Q, 2Q, \ldots\}$, $n \geq m+1$, $(n+m) \in O$) has been shown to converge to Prandtl's two-dimensional exact solution. Prandtl's solution and the dynamic wake model both include two-dimensional approximations. Prandtl's solution neglects inboard behavior by modelling the edge of semi-infinite vortex sheets. The original dynamic wake model neglects the tilt-angle of the thrust, induced-velocity and vorticity vectors. Both modelling approximations neglect the inboard behavior. The current formulation, with the appropriate weighting function in the mass-matrix, approximates the effect of the inboard behavior allowing for good correlation with the two-dimensional exact solution. The phenomena present in Goldstein's three-dimensional solution at the far inboard blade region is not captured by the current form of the dynamic wake models. A best-fit empirical factor, k, could be chosen for strong correlation with Goldstein's solution, but convergence will only occur at the medial and outboard blade regions. Further research into modelling the three-dimensional effects at the far inboard region will provide more utility than scaling the results with a smaller empirical factor, k.

Future Work

The physical phenomena at the inboard blade region affects the entire propeller system more significantly for small tip-speed ratios, $\mu_0 \approx 5$. Correspondingly, proper modelling of this inboard phenomena becomes important to achieve good correlation with the exact solution. Correlation can also be improved for cases where the inboard effects are less prominent, but still present, by appropriately modelling inboard behavior. Phenomena at the inboard region may also be important for skewed flow, such as forward flight. It is hypothesized that modes, neglected in the current dynamic wake model ($\hat{\tau}^{mc}_{m-j}$, $\hat{\tau}^{ms}_{m-j}$, $\hat{\alpha}^{m}_{m-j}$, $\hat{\beta}^{m}_{m-j}$ for $m \geq 0$ and $j \geq 1$) will capture the inboard blade phenomena present in Goldstein's solution. If this hypothesis proves true, it will allow for the addition of a new partition of mode shapes to make the dynamic wake model more comprehensive. Proper modelling of this inboard behavior with physically representative mode shapes should correspondingly affect the medial and outboard behavior, and improve the solution space of the dynamic wake model.

Additional modes, different in character than those currently used, should also allow the dynamic wake model to generate smoother solution results. The current formulation produces solutions that converge with some slight oscillatory behavior, which is not filtered out with additional higher order terms. Solutions with the new mode shapes should produce better convergence to the exact solution, and filter out the oscillations present in the above results.

Further work should also be done to better understand the idealized system that Goldstein studied (Ref 6). The reverse problem, with optimal induced velocity at the vortex sheets, was solved in this work. Goldstein solved for the velocity field between the vortex sheets, and then determined the circulation from this velocity field solution. Goldstein's velocity field solution can also be used for comparison to the forward problem solutions of the dynamic wake model.

The results presented are reproductions of results for an idealized propeller system. The idealized system does not include blade dynamics, airfoil lift characteristics, a root cutout, or interference due to the propeller nacell. Blade dynamics are important for studying coupled dynamic-aerodynamic systems, but the current project is not intended to focus on such a coupled system. Higher fidelity airfoil lift characteristics would probably not affect the results significantly (Ref 17). The above research results show success in modelling propeller aerodynamics for a large vortex shedding angle (small tip-speed ratio). Properly modelling an idealized propeller requires addressing the phenomena at the blade root, but real propeller systems have a root cutout and a nacell. Further work should be done to determine how to appropriately model real propellers, which consist of coupled systems but do not have lifting surfaces at $\bar{r} = 0$.

Acknowledgments

The work presented in this article was sponsored by the Boeing/Washington University Graduate Engineering Education and Research Partnership, by NRTC funding granted to the Georgia Tech/Washington University Center for Excellence in Rotorcraft Technology, and by the Army Research Office (Technical Monitor: Tom Doligalski).

References

[1] Holt Ashley and Marten Landahl. *Aerodynamics of Wings and Bodies*. Dover Publications, New York, NY, paperback edition, 1965.

[2] Ed Barocela, David Peters, Krish Krothapalli, and J.V.R. Prasad. The effect of wake distortion on rotor inflow gradients and off-axis coupling. In *AIAA Atmospheric Flight Mechanics Conference*, number AIAA-97-3579, August 11-13 1997. New Orleans.

[3] V.E. Baskin, L.S. Vil'dgube, Ye. S. Vil'dgube, and G.I. Maykapar. Theory of the lifting airscrew. translation NASA TT F-823, National Aeronautics and Space Administration, Washington D.C., February 1976. Translation of "Teoriya Nesushchego Vinta", edited by A.K. Martynov, Moscow, Mashinostroyeniye Press, 1973, pp.1-364., Translated by W.Z. Stepniewski, Transcribed by W.L. Metz.

[4] A. Betz and L. Prandtl. Schraubenpropeller mit ger-

ingstem energieverlust. *Goettinger Nachrichten*, pages 193–217, March 1919.

[5] H. Glauert. *Aerodynamic Theory: A General Review of Progress*, volume IV, chapter Division L, Airplane Propellers, pages 169–368. Dover Publications, Inc., New York, NY, dover edition edition, 1963.

[6] Sydney Goldstein. On the vortex theory of screw propellers. In *Proceedings of the Royal Society of London. Series A, Containing Papers of a Mathematical and Physical Character*, volume 123 of *792*, pages 440–465. The Royal Society, April 6 1929.

[7] David Fernandez Gomez. Convergence of a finite-state wake to the exact solution for an ideal propeller. Master of science thesis, Saint Louis University, St. Louis, Missouri, 2000.

[8] Steven R. Hall and Kyle Y. Yang. Helicopter rotor lift distributions for minimum-induced power loss. *Journal of Aircraft*, 31(4):837–845, July-August 1994.

[9] Chengjian He. *Development and Application of a Generalized Dynamic Wake Theory for Lifting Rotors*. Doctor of science thesis, Georgia Institute of Technology, Atlanta, Georgia, July 1989.

[10] Alan Jeffrey and Daniel Zwillinger, editors. *Table of Integrals, Series, and Products*. Academic Press, San Diego, California, sixth edition, 2000.

[11] Wayne Johnson. *Helicopter Theory*. Dover Publications, New York, NY, paperback edition, 1984.

[12] Stephen M. Makinen. *Applying Dynamic Wake Models to High Swirl Velocities for Optimal Propellers*. Doctor of science thesis, Washington University, St. Louis, Missouri, December 2004.

[13] K.W. Mangler. Calculation of the induced velocity field of a rotor. *Royal Aircraft Establishment*, (Aero 2247), September 1948.

[14] Jorge Morillo. *A Fully Three-Dimensional Unsteady Rotor Inflow Model from a Galerkin Approach*. Doctor of science thesis, Washington University, St. Louis, Missouri, December 2001.

[15] Jorge Morillo and David A. Peters. Velocity field above a rotor disk by a new dynamic inflow model. *Journal of Aircraft*, 39(5), September-October 2002.

[16] Robert A. Ormiston and David A. Peters. Hingeless rotor response with nonuniform inflow and elastic blade bending. *Journal of Aircraft*, 9(10):730–736, October 1972.

[17] David A. Peters and Chengjian He. A closed-form unsteady aerodynamic theory for lifting rotors in hover and forward flight. In *43rd Annual National Forum of the American Helicopter Society*, pages 839–866, St. Louis, Missouri, May 18-20 1987. American Helicopter Society.

[18] David A. Peters and Chengjian He. Correlation of measured induced velocities with a finite-state wake model. *Journal of the American Helicopter Society*, 36(3):59–70, July 1991.

[19] Dale M. Pitt. *Rotor Dynamic Inflow Derivatives and Time Constants from Various Inflow Models*. Doctor of science thesis, Washington University, St. Louis, Missouri, December 1980.